A methodology for microstructural evaluation of unsaturated flow phenomena by in-situ UV-flow freezing

Staal, Jeroen; Caglar, Baris; Michaud, Véronique

DOI
10.1002/pc.29448

Publication date
2025

Document Version
Final published version

Published in
Polymer Composites

Received: 6 November 2024 | Revised: 5 December 2024 | Accepted: 13 December 2024

DOI: 10.1002/pc.29448

RESEARCH ARTICLE

Polymer COMPOSITES WILEY

A methodology for microstructural evaluation of unsaturated flow phenomena by in-situ UV-flow freezing

Jeroen Staal[1] | **Baris Caglar**[2] | **Véronique Michaud**[1]

[1]Laboratory for Processing of Advanced Composites (LPAC), Institute of Materials, Lausanne, Switzerland

[2]Aerospace Structures and Materials Department, Faculty of Aerospace Engineering, Delft University of Technology, Delft, The Netherlands

Correspondence
Véronique Michaud, Laboratory for Processing of Advanced Composites (LPAC), Institute of Materials, Ecole Polytechnique Fédérale de Lausanne (EPFL), Station 12, Lausanne CH-1015, Switzerland.
Email: veronique.michaud@epfl.ch

Funding information
Swiss National Science Foundation, Grant/Award Number: SNF n° 200021_182669

Abstract

Microstructural analysis of resin flow in liquid composite molding is impeded by the absence of a characterization method that possesses both the required spatial and time resolution to capture the ongoing phenomena. An optimized UV-flow freezing methodology is presented to rapidly capture dynamic flow behavior, followed by high-resolution micro-computed tomography (μCT) imaging to extract the flow front morphology. Optimisation of the resin strongly enhances the photopolymerisation kinetics, reducing the gelation time by up to 56%, while an adequate postcuring procedure at moderate temperature is proposed by introducing radical induced cationic polymerization. Additives are identified to facilitate facile variation of the capillary number while distortions of the flow front morphology are minimized by finetuning the experimental procedure. μCT imaging allows for a micron-scale through-thickness assessment of unsaturated flow at range of flow regimes corresponding to both capillary- and viscous-dominated flow regimes while the corresponding saturation curves were derived by segmentation of the resulting images.

Highlights

- An optimized method for evaluating microstructural flow in fibrous preforms.
- Optimisation of the resin composition allows for fast UV-photopolymerisation.
- Additives identified for facile variation of the capillary number.
- Visualization of "frozen" microstructural flow by micro-CT analysis.
- Applicable to broad range of flow conditions that normally cannot be captured.

KEYWORDS

CT analysis, liquid composite molding, microstructural analysis, polymer-matrix composites (PMCs), resin flow

1 | INTRODUCTION

Liquid composite molding (LCM) techniques are often the preferred choice for composite processing as they allow for good part qualities at limited cost and production times compared to autoclave molding.[1] LCM processes consist of two main phases: a first phase where fabric stacks are infiltrated by a liquid monomer resin, followed by a second phase with thermal curing of the polymer. During the impregnation phase, as the reinforcement textiles are

generally made of yarns that are assembled into a textile, forming a porous medium with a dual-scale porosity,[2,3] many studies have shown that the quality of the final composite, in terms of void content and void location, strongly depends on the flow conditions, with a decreasing then increasing void content for increasing flow speed, all conditions remaining similar.[4–7] This is very critical for part manufacturing, since the uncontrolled presence of porosity in the part can lead to a deterioration of the mechanical properties of the resulting composite.[2,7–12] Understanding what phenomena dictates this behavior, and if possible being able to relate the liquid resin properties, and the reinforcement nature and architecture to predict the optimal flow front speed has been the object of intense research during the past 20 years, yet still lacks simple and practical methods to compare the morphology of the flow front during flow experiments, and the predictions.

Dual-scale flow behavior is generally related to the balance of capillary and hydrodynamic forces that are acting on the infiltrating resin in the porous medium.[2,11–13] In a capillary-dominated flow regime, when the overall flow velocity is rather low, the flow typically proceeds faster within the intra-yarn spaces, as it is driven by capillary forces (if the resin wets the fibers, which is generally the case) than in the inter-yarn regions. Flow patterns are inversed, on the other hand, when hydrodynamic forces dominate over capillary forces, so that the flow proceeds faster in the large inter-yarn regions than within the tows. This is often the case in part manufacturing under pressure such as in resin transfer molding. optimum conditions induce an equilibrated flow in the inter- and intra-yarn regions, which is reported to yield the lowest void content.[11] The capillary number (Ca), defined as:

$$Ca = \frac{v\eta}{\sigma_{lv}}, \tag{1}$$

where v is the resin velocity, η the dynamic viscosity and σ_{lv} the liquid-vapor surface tension, has been used (sometimes including in the denominator the cosine of a static contact angle θ, which is not possible for viscous resins for which this angle changes a lot with flow speed), following methods developed in soil science,[2,14–16] to describe the range of infiltrating flow front patterns. Several researchers have observed the presence of an optimum capillary number Ca_{opt}, which should correspond to the formation of an equilibrated flow with a minimum void content.[4,6,7,17–20] To prove this however, a direct observation of the flow front, rather than a post-mortem void content measurement, should be used.

Numerous characterization methods have thus been proposed to gain an improved visualization of dual-scale flow behavior. Several rapid imaging methods have been developed to capture the flow front, based on optical methods,[21–27] ultrasound,[28–31] magnetic resonance,[32–34] or the recently proposed x-ray phase contrast imaging,[35,36] which provided an improved understanding of unsaturated flow behavior on a macroscopic level; however, their spatiotemporal resolution is typically insufficient to capture the ongoing phenomena on a microstructural level. The exceptional spatial resolution of synchrotron micro-computed tomography (μCT) made it possible to observe unsaturated flow in fiber bundles[37–40] and later fibrous preforms[41] with an unprecedented accuracy. However, the slow imaging rates significantly limited the flow conditions that can be captured accurately.

It would be of high interest to stop the flow inlet and thus observe the flow front in a static mode to better elucidate the local contact angles and resin front morphology, however this is not possible in LCM in part due to the presence of capillary effects and remaining pressure gradients, which strongly modify the flow front before curing takes place. This was shown to be possible for flow of liquids that can solidify rapidly, such as metals, or water.[42] Caglar et al.[43] were the first ones to develop a UV-flow freezing methodology where an infiltrating resin is in-situ photopolymerised to 'freeze' the dynamic flow and thereby removed constraints on the time resolution for analysis by high-spatial resolution characterization methods. Neitzel & Puch[44] employed this methodology combined with optical analysis to relate the unsaturated flow length to the flow conditions. Although these reports have demonstrated the potential of the UV-flow freezing methodology, its use for microstructural flow analysis could not be fully demonstrated since freezing times, governed by the UV-photopolymerization kinetics and the experimental configuration, were still too long to obtain an accurate representation at this scale. In the meantime, the field of photopolymerisation has greatly evolved, with improved formulations and UV lamp technologies.[45,46] In this work, we propose to advance this flow-freezing methodology by enhancing the resin cure kinetics and establish a procedure combined with μCT analysis of frozen dual-scale flow fronts. Combined with identified additives to facilitate variation of the Ca, this work paves a way for the use of UV-flow freezing as an efficient experimental method toward an improved understanding of microstructural flow behavior.

2 | EXPERIMENTAL METHODS

2.1 | Resin preparation

UV-photopolymerisable resin formulations were based on a 3,4-epoxycyclohexylmethyl-3′,4′-epoxycyclohexane

carboxylate (ECC) resin (UviCure S105, Lambson, United Kingdom). Cationic photoinitiator p-(octyloxyphenyl)phenyl iodonium hexafluorostibate (IOC-8 SbF_6^-, ABCR, Germany) and photosensitiser isopropylthioxanthone (Genocure ITX, Rahn, Switzerland) were added in various amounts ranging from respectively 0.25 to 4 wt% and 0 to 1 wt%. Benzopinacol (Acros Organics, Belgium) was added at a concentration of 0.5 wt% to induce radical induced cationic polymerization (RICP)[47] for post-curing. Trimethylolpropane diallyl ether (TMPDE, TMPDE90, Perstorp, Sweden) and hexadecyl trimethoxysiloxane (HDMSi, Sigma Aldrich, Germany) were used as additives to alter respectively the viscosity and surface tension of the resin formulations. All resin components were mixed simultaneously under high shear rate until dissolved and resins were degassed under vacuum at room temperature for about 15 minutes prior to their experimental use.

2.2 | UV-flow freezing

UV-flow freezing experiments were carried out in a mold configuration as illustrated in Figure 1A, where a fabric stack is surrounded by a 1 mm thick metallic spacer and a silicone joint to prevent fluid leakage while being enclosed by two poly(methyl methacrylate) (PMMA) mold halves and metallic frames that facilitate closure of the mold. Inlet and outlet tubes were located at both ends of the mold cavity. The PMMA mold halves were in-house produced from pellets (Plexiglas, Evonik, Germany) to maximize their UV-transmission (see Supporting Information S4). Fabric stacks were made up of three 100 × 50 mm layers of E-glass 2 × 2 twill weave fabric (Suter Kunststoffe, Switzerland) with an areal density of 390 g/m^2, an ends/picks count of 6/6.7 cm^{-1} and a linear density of 340 and 272 tex in warp and weft, respectively. The fiber volume fraction in the fabric stack equalled was calculated as:

$$V_f = \frac{nA}{\rho t}, \tag{2}$$

where n denotes the number of fabric layers, A the areal density, ρ the bulk fiber density taken as 2.6 g/cm^3 and t the cavity thickness that equalled 1 mm. The fiber volume fraction was kept constant at 45% for all experimental conditions.

The experimental configuration for infiltration and UV-flow freezing is shown in Figure 1B. Resin impregnation was carried out under a range of constant flow rates using a Razel Scientific Instruments R-100e syringe pump. The inlet pressure and resin temperature were recorded by a Keller Series 35XHTT placed in-series between the syringe pump and the inlet. Impregnation was recorded by a camera (Canon EOS 700D). Resin infusion was manually stopped, and the UV-light was simultaneously applied when the flow front reached about two-thirds of the fabric length, after which the inlet tube was rapidly disconnected to release the resin pressure, and hence the hydrodynamic pressure, to minimize the residual propagation. The UV-irradiation was provided from two EXFO Omnicure UV-sources that were placed at opposing sides of the PMMA mold halves. Irradiation was carried out for 240 seconds at an intensity at the mold surface of ~200 mW/cm^2, followed by UV-photopolymerisation of the region behind the flow front. Fabrics were removed from the mold and placed in

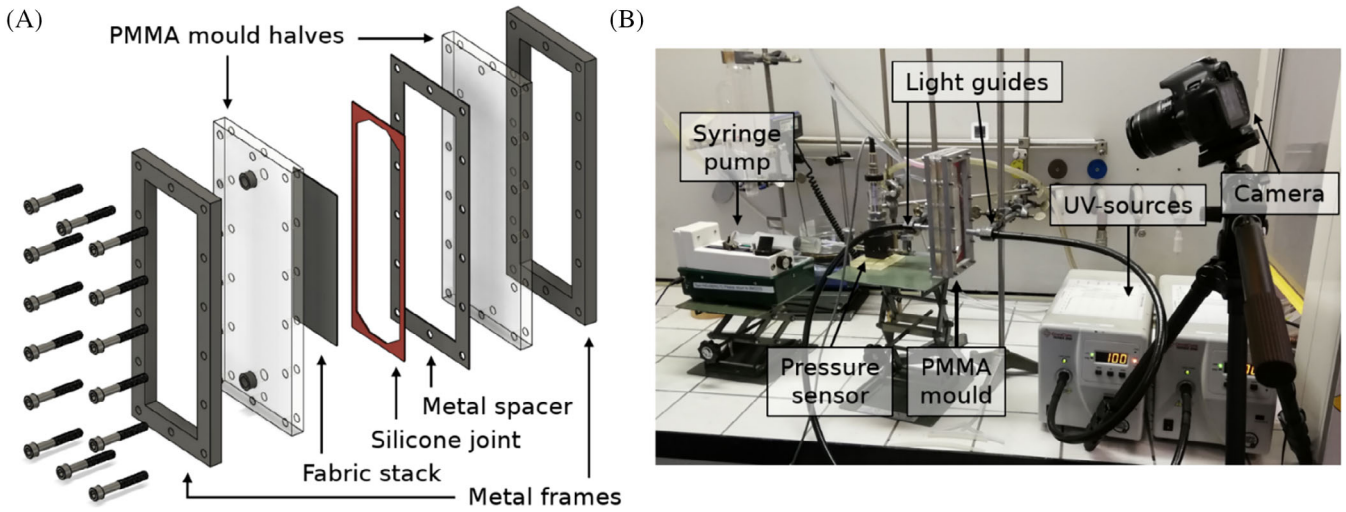

FIGURE 1 Experimental configuration for UV-flow freezing experiments: (A) exploded-view representation of the poly(methyl methacrylate) (PMMA) mold and (b) experimental setup for impregnation and UV-photopolymerisation.

an oven at 120°C for a minimum of 1 hour to ensure complete curing of the sample.

2.3 | Resin characterization

The rheological behavior of resin formulations was characterized using a TA instruments AR2000ex rheometer with a Peltier concentric cylinder setup in continuous shear mode. Temperatures were varied between 15 and 30°C at a rate of 0.1°C/min while shear rates were kept constant at 10 s^{-1}. The viscosity-temperature behavior was fitted with an Arrhenius equation[48,49]:

$$\eta(T) = A\exp\left(\frac{E_a}{RT}\right), \tag{3}$$

where η is the resin viscosity, A the pre-exponential factor, E_a the activation energy, R the molar gas constant and T the resin temperature. The resulting fits showed good correlation with the experimental data and were used to estimate the resin viscosity in UV-flow freezing experiments.

The photocuring behavior of resin formulations was assessed using a photorheology configuration where a sample was oscillated by a 20 mm metallic top plate while being irradiated through an in-house produced PMMA bottom plate. Measurements were carried out in oscillation mode at an oscillation frequency of 1 Hz, a gap of 200 μm and a strain of 1%. UV-intensities were recorded prior to each measurement using a Control-cure Silverline UV radiometer. The induction time was defined as the time between the start of irradiation and the onset of the viscosity increase while the gelation time was defined as the time where the phase angle between the viscous and elastic moduli, that is, tan(δ), equalled one. An exemplary photorheology curve is shown in Supporting Information S1.

Post-curing strategies were developed by means of differential scanning calorimetry (DSC) using a TA Instruments DSC Q100. Aluminum hermetic pans were filled with ~2 to 3 mg of resin and an empty pan was used as reference. Dynamic heat flow measurements consisted of a temperature ramp from −20 to 270°C at a rate of 5°C/min. Polymerization enthalpy was determined by integration of the heat flow signal after baseline correction by a third order polynomial. Quasi-isothermal procedures consisted of an initial temperature ramp from −20 to 120°C at 5°C/min after which the sample was kept at 120°C for 1 hour to simulate post-curing in an oven.

UV-absorbance of the different constituents was characterized by UV–vis spectrophotometry (Varian Cary 50 Bio) in a 10 mm quartz cuvette after dissolution in dichloromethane at a concentration of 0.05 mM. The transmittance of in-house produced PMMA was recorded using the same apparatus on 12 × 50 × 50 mm plates after polishing their surface. Spectra were recorded over a range of 250–800 nm at an interval of 1 nm. The liquid-vapor surface tension was characterized using the pendant drop method at ambient temperature using a Krüss DSA30 drop shape analyzer. Resulting surface tension values were averaged over a minimum of three recordings and were assumed to be constant over the considered temperature ranges for in-situ flow freezing experiments.

2.4 | Flow front

Flow fronts morphologies were characterized by μCT using a RX Solutions Ultratom. Samples were cut in strips of ~15 mm after which a contrasting agent, composed of 60 g zinc iodide dissolved in 10 mL of ethanol, 10 mL of water and 10 mL of Kodak Photo-Flo 200,[50] was deposited near the flow front region to enhance the contrast between the polymer and air interfaces and hence allow for identification of the flow front. Acquisitions were made with a voltage of 60 kV and an x-ray current of 85 μA. The voxel size was fixed to 3.5 μm while the scanned sample volume was adapted based on the length of the unsaturated flow front region. Image analysis was carried out using the Avizo software package (Thermo Fisher Scientific). The raw data was first filtered using a non-local means filter with a search window of 10 pixels, similarity value of 0.2. Saturated and unsaturated regions of the resulting μCT recordings were manually segmented based on their grey-scale appearance, followed by voxelisation by an in-house developed Python script. Saturation curves were calculated for each slice in front direction as:

$$S = 1 - \frac{n_{vxl}}{n_{vxl,tot}}, \tag{4}$$

where S denotes the saturation level, n_{vxl} the number of voxels identified as unsaturated in a slice and $n_{vxl,tot}$ the total number of voxels in that slice. Saturation levels for individual fabric slices were calculated by dividing the sample thickness into three equal height horizontal sections corresponding to the bottom, centre, and top fabric layers.

3 | RESULTS AND DISCUSSION

3.1 | Optimisation of the UV-curable resin formulation

Capturing an accurate representation of the dynamic flow behavior by UV-flow freezing requires fast setting of

the resin and hence fast UV-photopolymerisation kinetics. Figure 2A,B shows that an increase of the photoinitiator concentration resulted in a strong decrease of the gelation time (Figure 2B) while the slightly increasing trend recorded for the induction time (Figure 2A) was attributed to the increased light attenuation. A concentration of 1 wt% was chosen as the optimum trade-off between these two trends. The presence of a photosensitising compound in the resin resulted in a further decrease of both the induction and gelation times, as shown in Figure 2C,D, respectively. A small addition of photosensitiser (i.e., a change from the molar ratio of 0–0.1) resulted in a significant decrease in both induction time and gelation time while further increase of the molar ratio had a more incremental effect. A molar ratio between photosensitiser and photoinitiator of 0.25 was found to be the optimum, resulting in a decrease in the gelation time of up to 56%. Thus, the isopropylthioxanthone photosensitising compound was added to the resin formulation at a fixed concentration of 0.1 wt%.

The presence of glass fiber reinforcement in UV-flow freezing experiments was expected to induce significant scattering of the incoming UV-light. This makes complete monomer conversion unlikely to be achieved, especially within the fiber bundles. A thermal post-curing strategy was therefore developed to ensure maximum curing of the polymer and thereby to minimize the risk of inducing distortions in the frozen flow front morphology during the post-processing and analysis, in particular induced by the contrasting agent that was observed to dissolve and redistribute the fraction with limited cure degree in some instances. Dynamic DSC analysis in Figure 3A showed that the exothermic peak of a resin formulation containing ECC monomer, photoinitiator and photosensitiser was recorded at 143.50°C. The addition of benzopinacol as a free-radical (thermal) initiator, that is, inducing RICP,[47] significantly lowered the temperature required for thermal curing. A benzopinacol concentration of 0.5 wt% was found to be the optimum as it allowed for thermal polymerization with a high resulting curing degree, based on the total enthalpy of 552.7 J/g, at limited temperatures of 100–120°C while the concentration was sufficiently low to avoid the onset of frontal polymerization.[51] Simulation of the oven curing

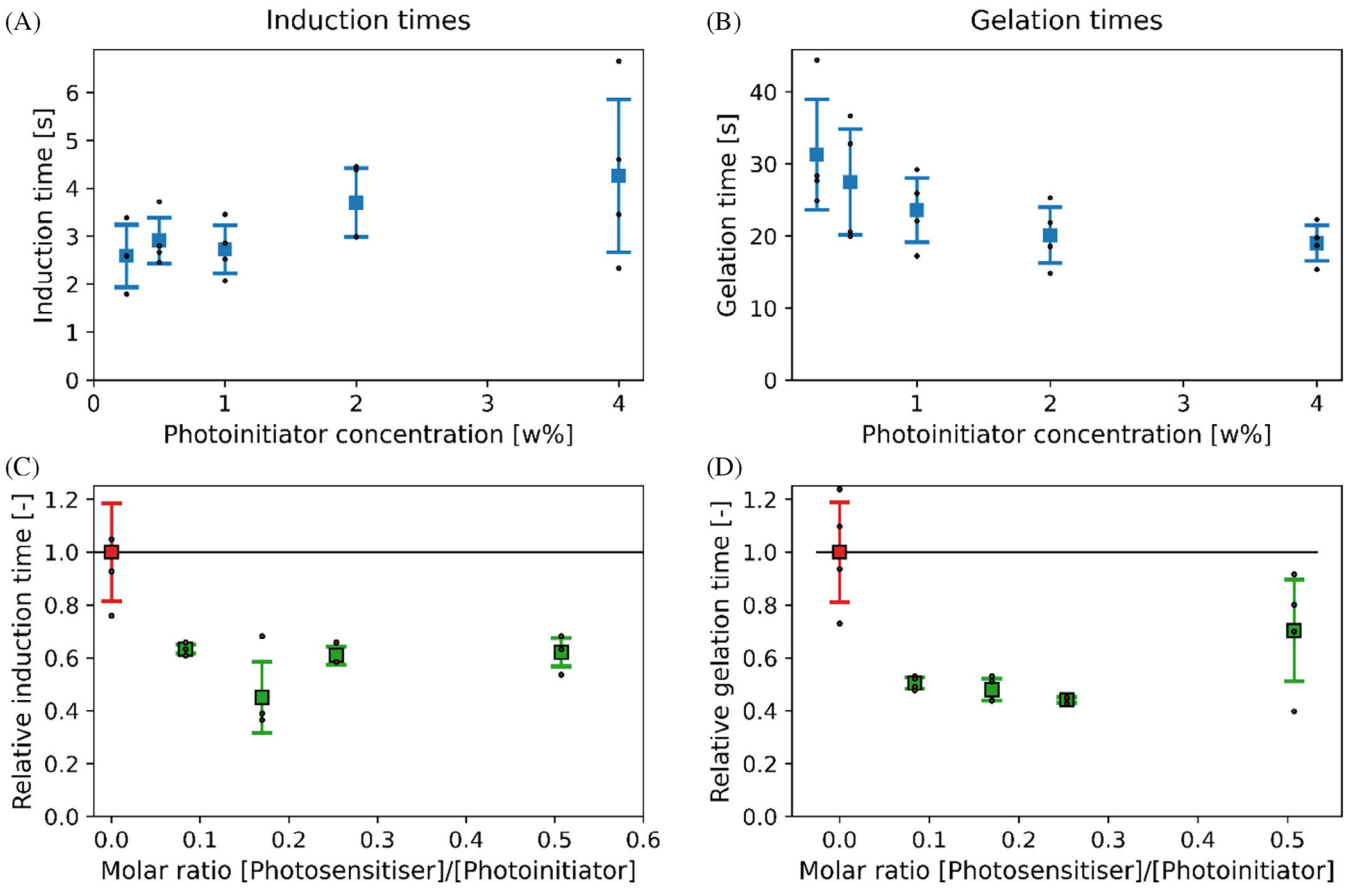

FIGURE 2 Photorheological assessment with varying resin compositions: (A) induction and (B) gelation times with varying photoinitiator content (and no photosensitiser) and (C) induction and (D) gelation times with varying molar ratios of photoinitiating and photosensitising compounds.

procedure at 120°C by a quasi-isothermal DSC procedure, shown in Figure 3B, confirms the benefit of the introduced RICP mechanism for postcuring. The resin formulation capable of RICP showed a large heat output when being kept at the isothermal temperature while the recorded polymerization enthalpy was significantly lower when no free-radical compound was added. Figure 4A moreover showed that the absorbance spectra of benzopinacol only slightly overlapped with the emission spectrum of the UV-source and hence is believed to be of negligible influence on the UV-photopolymerisation behavior of the developed resin composition.

An optimized resin composition was therefore concluded to be composed of 1 wt% IOC-8 SbF_6 photoinitiator, 0.1 wt% isopropylthioxanthone photosensitiser and 0.5 w% benzopinacol thermal initiator, as is also shown in Table 1. This resin system can achieve mechanical gelation, that is, the crossover point between the storage and loss moduli, within 13 seconds at UV-intensities >200 mW/cm^2 while viscosities of 10 Pa·s were typically attained within 10 seconds. Figure 4B shows that the photocuring behavior of the developed resin is highly dependent on the incoming light intensity and a significant decrease was observed at low UV-intensities, that is, <100 mW/cm^2. The latter might be significant due to the attenuation and scattering induced by the presence of glass fibers in UV-flow freezing experiments, especially within the yarns where the density of fibers is the highest, and it supports the need of the dedicated postcuring process.

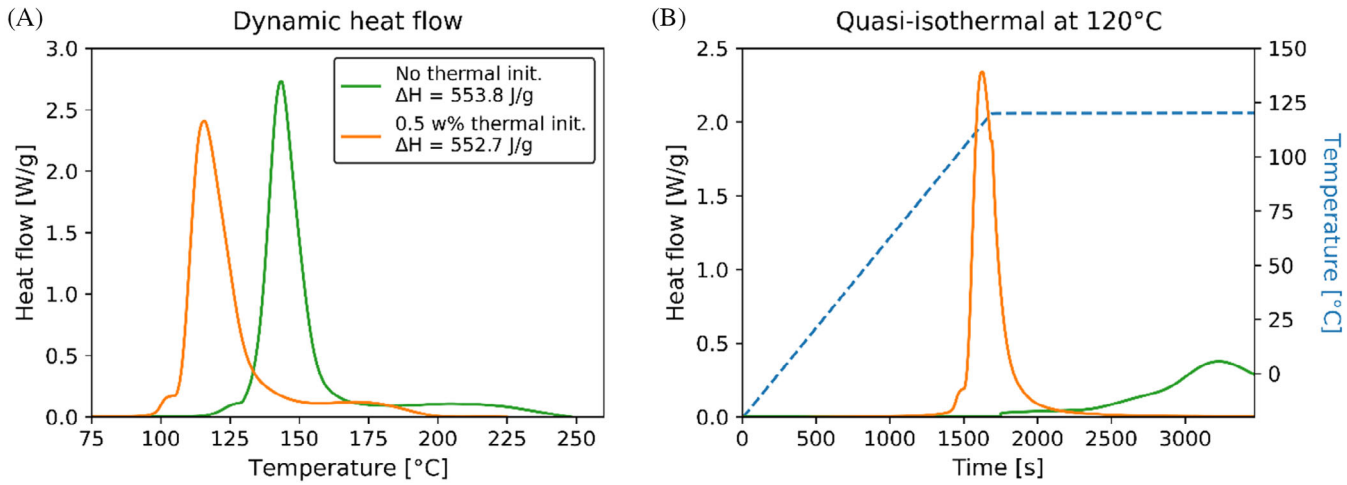

FIGURE 3 Differential scanning calorimetry (DSC) analysis of postcuring of resins with and without thermal initiating compound: (A) dynamic heat flow measurements and (B) simulation of oven curing by a quasi-isothermal measurement at 120°C. The legend in (A) applies to both figures.

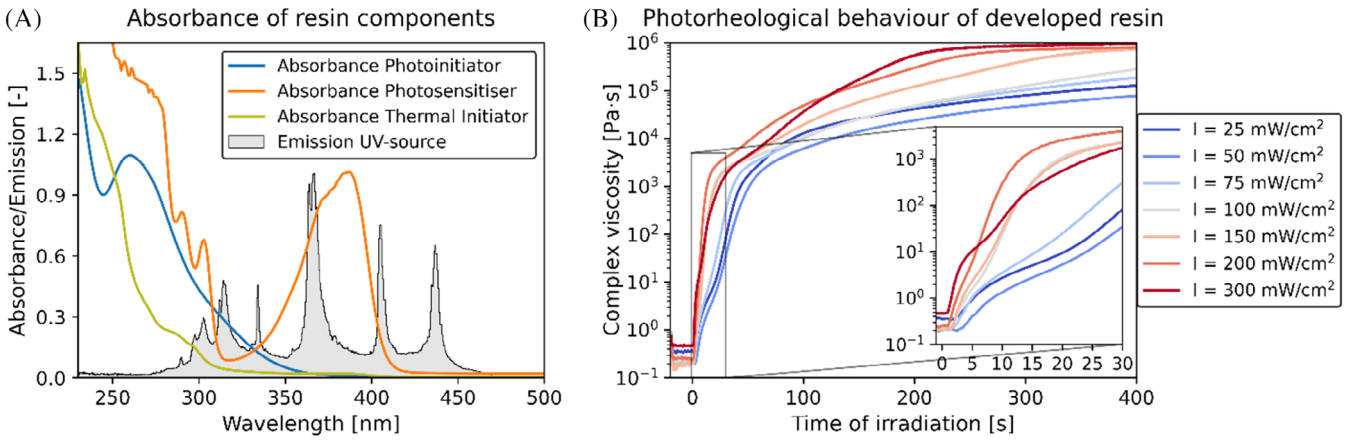

FIGURE 4 (A) Absorbance of the different components of the developed UV-photopolymerisation resin. Resin constituents were recorded after dissolution in dichloromethane at a concentration of 0.05 mM. (B) Photorheological behavior of the optimized photopolymerisable resin system with varying UV-irradiation intensities.

3.2 | Enabling variation of the capillary number via additives

To explore the potential for broader use of the UV-flow freezing methodology, for example, toward gaining an improved understanding of the governing *Ca* and the flow front morphology, modification of the resin formulation to facilitate variation of the *Ca*, that is, by changing the viscosity or the surface tension, was desired. For this purpose, two suitable additives were identified. TMPDE was identified as a suitable diluent for the optimized resin system while, acting as a charge transfer agent, TMPDE can also accelerate the initial polymerization kinetics and hence potentially reduce the freezing time. The inability to incorporate TMPDE in the polymer network however limits the structural integrity of the frozen flow front which, following photorheological characterization shown in Supporting Information S2, imposes an upper limit of 20 wt% of TMPDE that could be added to the system while maintaining the rigidity of the frozen flow front. Variations of the liquid-vapor surface tension were induced by the addition of minor concentrations of HDMSi. The addition of 5 wt% of HDMSi was sufficient to reduce the surface tension of the resin formulation from 32.2 mN/m compared to 39.7 mN/m at a concentration of 1 wt% HDMSi, while only inducing subtle variations in the resin viscosity. The low concentrations of HDMSi were moreover believed to be of negligible influence on the cure kinetics and the rigidity of the frozen flow front. The combination of additives TMPDE and HDMSi for the proposed UV-flow freezing formulation allows for facile tailoring of the liquid-vapor surface tension (Figure 5A) and the resin viscosity (Figure 5B) and thereby the Ca. This is believed to be strongly beneficial for the future use of the proposed methodology.

TABLE 1 Overview of optimized resin formulation.

Compound	Concentration (wt%)
Epoxide–ECC	98.4
Photoinitiator–IOC-8 SbF_6	1
Photosensitiser–Isopropylthioxanthone	0.1
Thermal initiator–Benzopinacol	0.5

3.3 | UV-flow freezing and microstructural analysis

Optimisation of the mold configuration and impregnation procedure, discussed in more detail in Supporting Information S4, further ensured the accuracy of the representation obtained after UV-flow freezing of the dynamic flow front. Optical recordings of frozen flow fronts at different *Ca* values are shown in Figure 6. These *Ca* values were reported by Caglar et al.[43] to correspond to respective capillary-dominated ($Ca \approx 3.5 \cdot 10^{-4}$), equilibrated ($Ca \approx 9.6 \cdot 10^{-4}$) and viscous-dominated flow regimes ($Ca \approx 4.06 \cdot 10^{-3}$). Except for a color change due to the change of refractive index upon curing, the optical recordings showed no apparent differences in front morphology during impregnation, after in-situ UV-photopolymerisation and after post-curing. Moreover, by assessing the residual front propagation in an uncured system, also shown in Supporting Information S4, the fronts were found to propagate with velocities of approximately 5.3, 7.1, and 70.9 μm/s for the respective capillary-dominated, equilibrated and

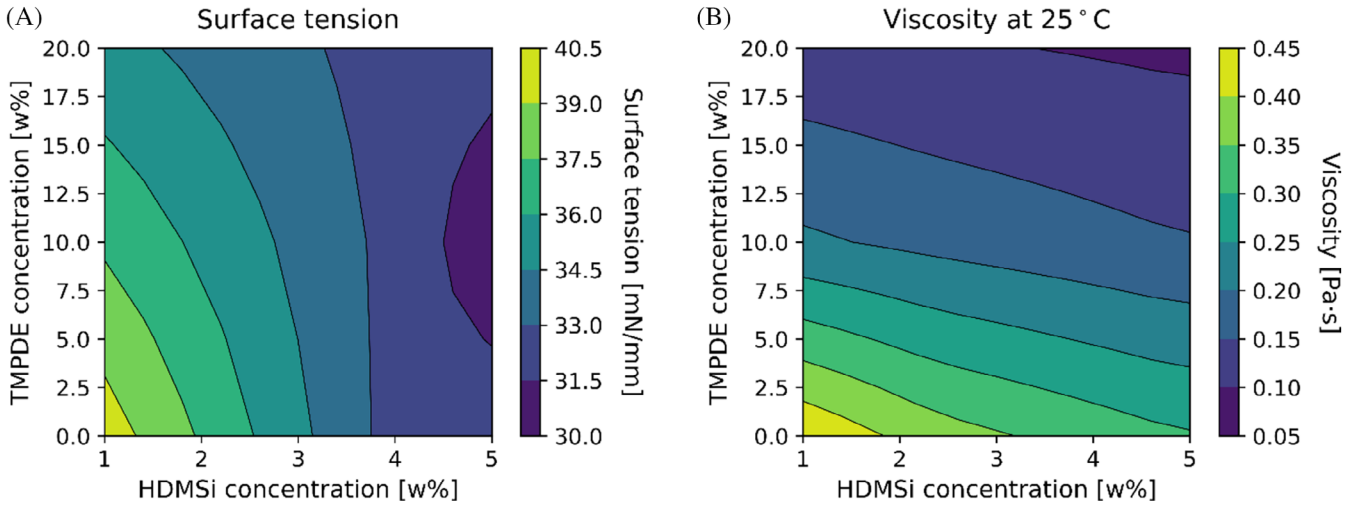

FIGURE 5 Influence of additives trimethylolpropane diallyl ether (TMPDE) and hexadecyl trimethoxysiloxane (HDMSi) on the (A) liquid-vapor surface tension and (B) viscosity at 25°C of the resin formulation.

viscous-dominated flow regimes. These residual velocities mean a reduction of 83.4%–94.0% from the initial propagation velocity while the rapidly increasing viscosity induced by UV-photopolymerisation is believed to further slow down the residual propagation. It was therefore believed that the developed experimental procedure was sufficient to minimize undesired distortions of the flow front morphology during the freezing of the resin.

The obtained flow front morphologies showed minor differences as compared to those reported by Caglar et al.[43] These are primarily attributed to the increased number of textile layers that were used in this work, limiting the significance of wall-effects,[11,52,53] and differences in the impregnation strategy that was used. Some subtle color changes in the region behind the flow front could be observed in Figure 6, which include the suggested formation of intra-yarn porosity at a $Ca \approx 4.06 \cdot 10^{-3}$ or inter-yarn voids at the other flow conditions. Optical observation of these defects is however complicated by the change in refractive index, combined with the potential influence of wall-effects. This further supports the limitation of UV-frozen flow analysis by means of optical characterization, while it should mainly be applied for characterizing the flow front region.

μCT imaging of the UV-frozen flow fronts allowed, for the first time, for through-thickness visualization and identification of unsaturated flow at a micron-scale for all the considered flow regimes. The acquired three-dimensional representations, shown in Figure 7, already indicate differences between the different flow regimes; the unsaturated flow region recorded for capillary-(Figure 7A) and viscous-dominated (Figure 7C) flow regimes showed distinct sharp features as a result of the preceding flow while the flow corresponding to an equilibrated regime (Figure 7B) appeared to be smoother. The precise experimental conditions from which these flow front morphologies were obtained can be found in Supporting Information S5 while through-thickness visualization of the acquired μCT images can be found in the Supplementary Information.

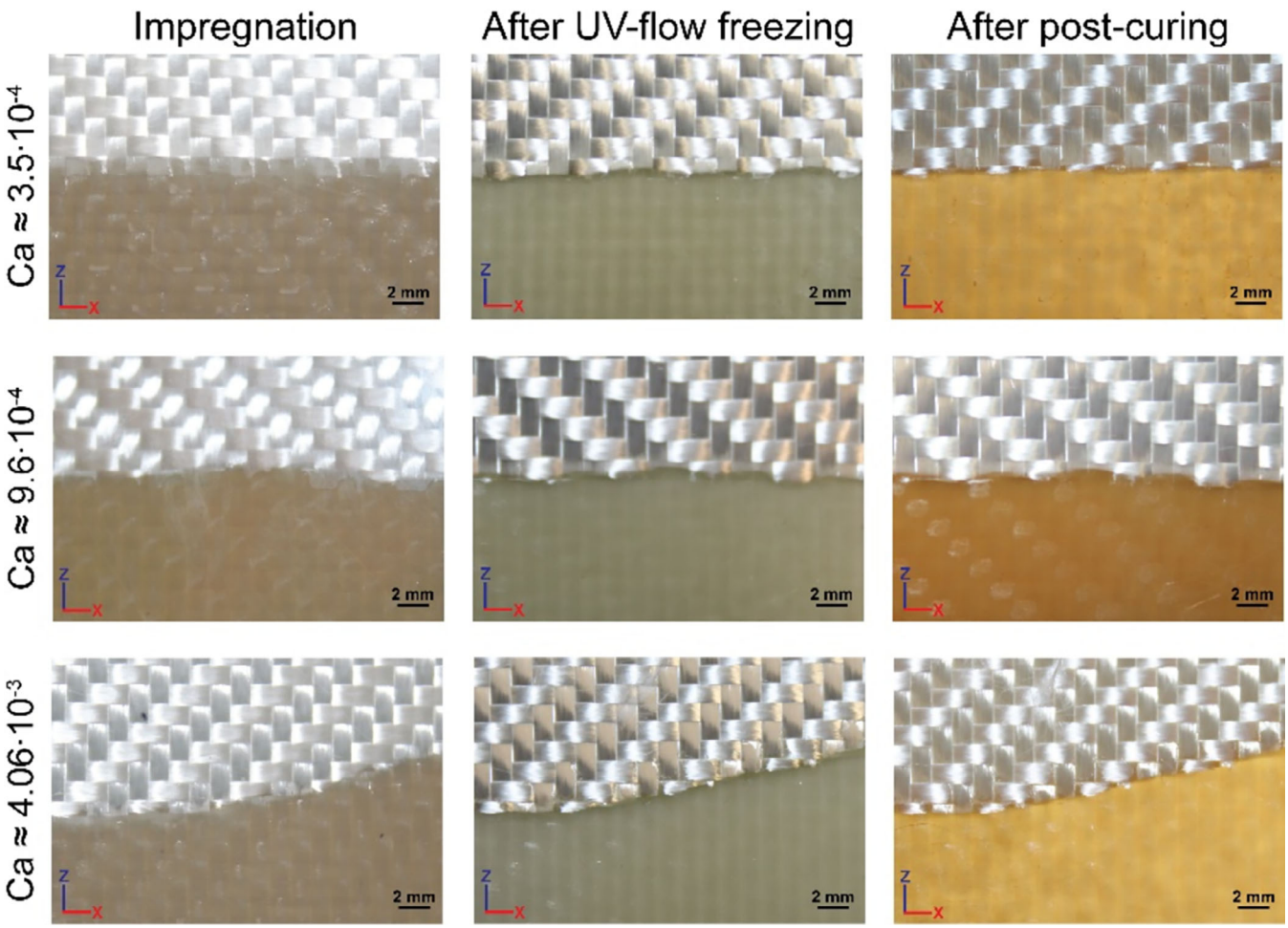

FIGURE 6 Optical imaging of flow front morphologies related to varying capillary numbers. Front morphologies were optically recorded during resin infiltration, after UV-flow freezing and after post-curing.

A representative μCT slice in Figure 8 shows that the combination of the chosen voxel size of 3.5 μm and the applied contrasting agent resulted in a clear separation between the saturated and unsaturated regions. Inter-yarn voids could be observed within the saturated region if sufficiently large in size while the polymer-air x-ray contrast was insufficient to detect intra-yarn voids. Several artifacts complicated the segmentation of the unsaturated and saturated flow regions. Residual air pockets in the unsaturated region that were not filled with contrasting agent appeared as voids in this region while identification of the front was in some cases complicated by its limited contrast in regions with a high fiber density, for example, within transverse yarns as illustrated in Figure 8. Finally, blurring effects of fibers spanning several voxels complicated their distinction from regions near the flow front with reduced concentrations of contrasting agents. Although further optimisation of the sample preparation and imaging could eliminate their presence, it was believed that the developed segmentation procedure was sufficient to circumvent any negative effects from these artifacts.

Saturation curves derived from the segmented μCT images in Figure 9A–C show the differences between the different flow conditions. The saturation curves of individual fabric layers were largely similar for all the assessed flow regimes. The minor delay of saturation for the centre layer was in some cases observed, which is attributed to a combination of the aforementioned wall-effects and a slightly reduced curing rate due to attenuation of the incoming UV-light by the neighboring fabric layers. This shift was however believed to be of negligible influence since the saturation curves were similar to those recorded for the outer fabric layers.

Further comparison between the saturation curves in Figure 9A–C shows that the curves transition from a bilinear trend at a $Ca \approx 3.5{\cdot}10^{-4}$ (Figure 9A) to a linear trend at $Ca \approx 9.6{\cdot}10^{-4}$ and $Ca \approx 4.06{\cdot}10^{-3}$ in Figure 9B,C, respectively, which is in agreement with the work of Teixido et al.[54] The initial segment of bilinear trend in Figure 9A corresponds to a capillary-dominated flow regime, as can be evidenced from the μCT capture shown in Figure 9D, is believed to correspond to the inter-yarn flow, while the following gradual decrease was attributed to extensive capillary wicking. It should be noted however that the relative ratio of these two phenomena is biased by the incapability to segment fibers from the intra-yarn flow

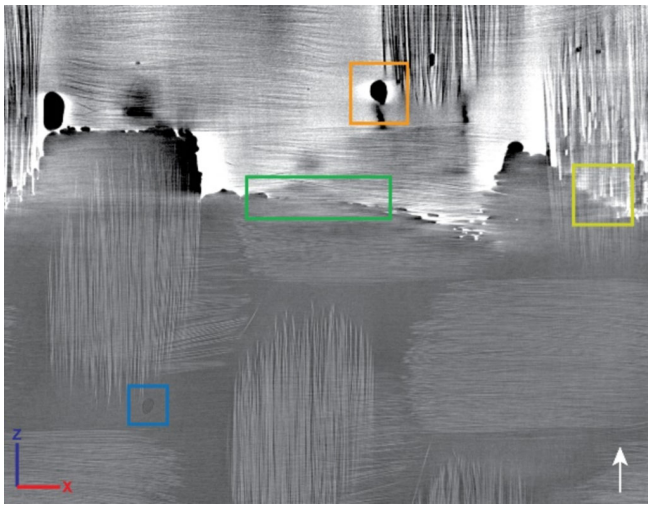

FIGURE 8 Representative slice of a μCT image indicating the recorded artifacts: (blue) an inter-yarn void, (orange) air pocket in a region with deposited contrasting agent, (green) polymer-air interface in a transverse yarn and (olive) blurring effects. The white arrow on the bottom-right side indicates the direction of resin flow.

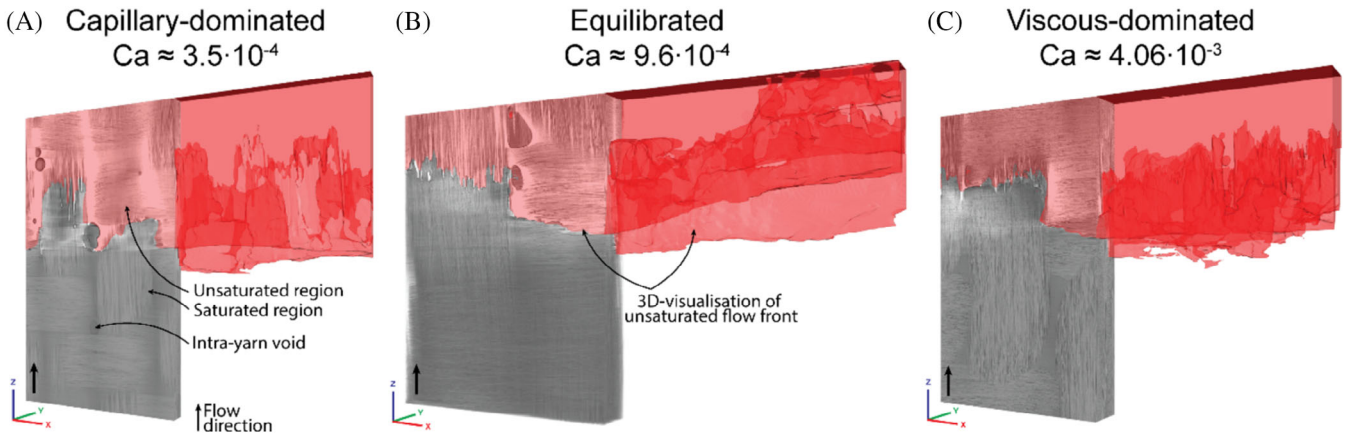

FIGURE 7 Three-dimensional representation of UV-frozen flow fronts recorded at different flow regimes: (A) capillary-dominated with a Ca ≈ $3.5{\cdot}10^{-4}$, (B) equilibrated with a Ca ≈ $9.6{\cdot}10^{-4}$, and (C) viscous-dominated with a Ca ≈ $4.06{\cdot}10^{-3}$. Flow direction is upwards in z-direction.

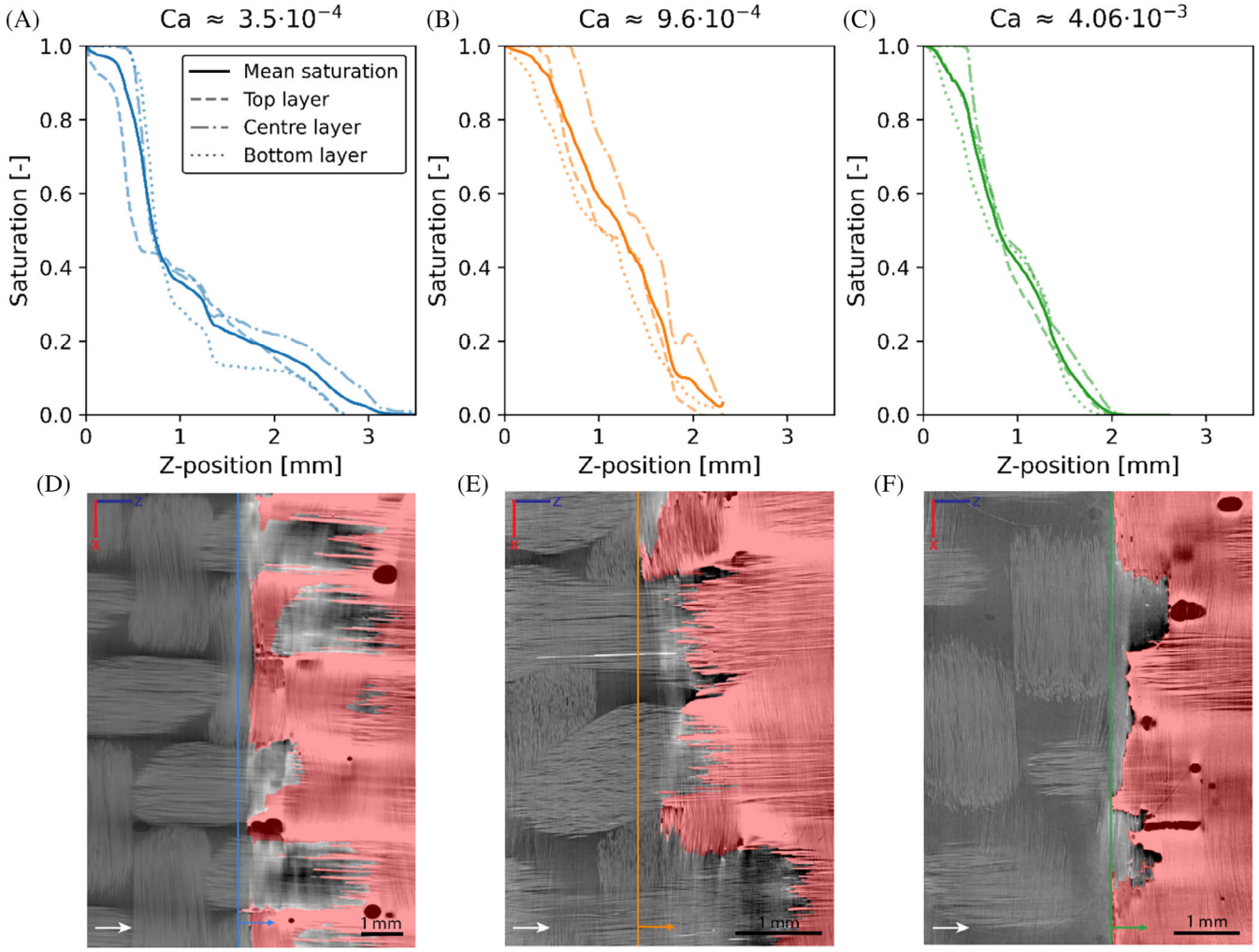

FIGURE 9 Saturation curves derived by μCT analysis of flow front morphologies at (A) capillary-dominated, (B) equilibrated and (C) viscous-dominated flow regimes. Bottom row: Representative slices of μCT images with the unsaturated region marked in red and a vertical line indicating the start of this region, corresponding to a position of 0 mm: (D) capillary-dominated, (E) equilibrated and (F) viscous-dominated flow regimes. Flow direction is indicated by a white arrow.

at the current μCT resolution and the inflection point should in reality be present at a lower saturation level. The combined use of the developed UV-flow freezing methodology and μCT was thus found able to visualize capillary wicking in LCM processing that can only be matched by the use of synchrotron-μCT, for example, as demonstrated by Castro et al.[41] The flow rates used for producing the flow fronts shown in Figure 9 however all exceed the limit observed by Castro et al.[41] above which blurring of the μCT recordings would occur, which further confirms the benefit of the presented methodology.

4 | CONCLUSION

A combination of UV-flow freezing and μCT was foreseen as a promising strategy to enable the microstructural evaluation at a wide range of dynamic flow conditions in LCM processing. Based on the methodology presented by Caglar et al.,[47] an optimized resin formulation was proposed. The induction time of the initial viscosity increase, corresponding to the onset of curing, and gelation time of UV-photopolymerisable resins were strongly decreased by tuning of the photoinitiator and photosensitiser concentrations while the addition of a free-radical thermal initiator was found beneficial for thermal post-curing of the UV-frozen flow fronts. Additives were identified to allow for facile variation of the viscosity and surface tension and hence the governing parameters of the capillary number. Optimisation of the experimental configuration using in-house produced PMMA mold halves, to maximize the UV-transmittance, impregnation under a constant flow rate and the rapid relaxation of the resin pressure upon the start of UV-flow freezing, to minimize

undesired distortions of the flow front morphology, contributed to accuracy of the resulting representation of dynamic flow behavior. μCT analysis of flow front morphologies produced at viscous-dominated, equilibrated and capillary-dominated flow regimes allowed for a volumetric assessment and the derivation of saturation curves. Strong capillary wicking could be observed at low values of the capillary number while the variability in the evolution of saturation correlated to features in the fabric architecture. These observations confirmed the potential of UV-flow freezing as a tool for microstructural evaluation of dynamic flow behavior bringing additional benefits such as a low cost and its ease of implementation, for example, compared to synchrotron-μCT.

Further assessment on the obtained representations of dynamic flow behavior, for example, by making a direct comparison between UV-flow freezing and dynamic (slow-)flow experiments, would validate the accuracy of the developed methodology and define the range of spatial resolutions that could be reached. Development of the methodology to observed intra-yarn flow, for example, to characterize dynamic contact angles, would further require estimations of the curing shrinkage. The UV-flow freezing methodology is envisioned to contribute to the understanding on the role of the capillary number in LCM as well as to study the role of the fibrous preform by variation of the fabric architecture and types.

ACKNOWLEDGMENTS

The authors acknowledge the support from the Swiss National Science Foundation (SNF n° 200021_182669). Gary Perrenoud is greatly thanked for his help during the μCT imaging and analysis.

DATA AVAILABILITY STATEMENT

The data that supports the findings of this study are available in the supplementary material of this article.

ORCID

Véronique Michaud https://orcid.org/0000-0001-5699-740X

REFERENCES

1. Ermanni P, Fratta C, Trochu F. *Molding: Liquid Composite Molding (LCM)*. Wiley Encyclopedia of Composites, Wiley-VCH; 2012. doi:10.1002/9781118097298.weoc153
2. Michaud V. A review of non-saturated resin flow in liquid composite moulding processes. *Trans Porous Media*. 2016;115:581-601. doi:10.1007/s11242-016-0629-7
3. Michaud V. Permeability properties of composite reinforcements. In: Boisse P, ed. *Composite Reinforcements for Optimum Performance (Second Edition)*. Woodhead Publishing Series in Composites Science and Engineering; 2021:443-472. doi:10.1016/B978-0-12-819005-0.00014-9
4. LeBel F, Fanaei AE, Ruiz E, Trochu F. Prediction of optimal flow front velocity to minimize void formation in dual scale fibrous reinforcements. *Int J Mater Form*. 2014;7:93-116. doi:10.1007/s12289-012-1111-x
5. Ruiz E, Achim V, Soukane S, Trochu F, Bréard J. Optimization of injection flow rate to minimize micro/macro-voids formation in resin transfer molded composites. *Compos Sci Technol*. 2006;66:475-486. doi:10.1016/j.compscitech.2005.06.013
6. Leclerc JS, Ruiz E. Porosity reduction using optimized flow velocity in resin transfer molding. *Compos Part A Appl Sci Manuf*. 2008;39:1859-1868. doi:10.1016/j.compositesa.2008.09.008
7. Zingraff L, Michaud V, Bourban PE, Månson JAE. Resin transfer moulding of anionically polymerised polyamide 12. *Compos Part A Appl Sci Manuf*. 2005;36:1675-1686. doi:10.1016/j.compositesa.2005.03.023
8. Park CH, Lebel A, Saouab A, Bréard J, Il Lee W. Modeling and simulation of voids and saturation in liquid composite molding processes. *Compos Part A Appl Sci Manuf*. 2011;42:658-668. doi:10.1016/j.compositesa.2011.02.005
9. Lundström TS, Gebart BR, Lundemo CY. Void formation in RTM. *J Reinf Plast Compos*. 1993;12:1339-1349. doi:10.1177/073168449301201207
10. Schell JSU, Deleglise M, Binetruy C, Krawczak P, Ermanni P. Numerical prediction and experimental characterisation of meso-scale-voids in liquid composite moulding. *Compos Part A Appl Sci Manuf*. 2007;38:2460-2470. doi:10.1016/j.compositesa.2007.08.005
11. Teixidó H, Staal J, Caglar B, Michaud V. Capillary effects in fiber reinforced polymer composite processing: a review. *Front Mater*. 2022;9:1-24. doi:10.3389/fmats.2022.809226
12. Mehdikhani M, Gorbatikh L, Verpoest I, Lomov SV. Voids in fiber-reinforced polymer composites: a review on their formation, characteristics, and effects on mechanical performance. *J Compos Mater*. 2019;53:1579-1669. doi:10.1177/0021998318772152
13. Gueroult S, Lebel-Lavacry A, Park CH, Bizet L, Saouab A, Bréard J. Analytical modeling and in situ measurement of void formation in liquid composite molding processes. *Adv Compos Mater*. 2014;23:31-42. doi:10.1080/09243046.2013.862383
14. Sahimi M. *Flow and Transport in Porous Media and Fractured Rock: from Classical Methods to Modern Approaches*. 2nd ed. Wiley-VCH; 2011. doi:10.1002/9783527636693
15. Hunt AG. *Percolation Theory for Flow in Porous Media*. Springer; 2005. doi:10.1007/b136727
16. Dullien FAL. Pore structure. *Porous Media, Fluid Transport and Pore Structure*. Academic Press; 1979.
17. Patel N, Lee LJ. Modeling of void formation and removal in liquid composite molding. Part I: wettability analysis. *Polym Compos*. 1996;17:96-103. doi:10.1002/pc.10594
18. Park CH, Lee W. Modeling void formation and unsaturated flow in liquid composite molding processes: a survey and review. *J Reinf Plast Compos*. 2011;30:957-977. doi:10.1177/0731684411411338
19. Kang MK, Il Lee W, Hahn HT. Formation of microvoids during resin-transfer molding process. *Compos Sci Technol*. 2000;60:2427-2434. doi:10.1016/S0266-3538(00)00036-1

20. Verrey J, Michaud V, Månson JAE. Dynamic capillary effects in liquid composite moulding with non-crimp fabrics. *Compos Part A Appl Sci Manuf*. 2006;37:92-102. doi:10.1016/j.compositesa.2005.04.011
21. Nordlund M, Michaud V. Dynamic saturation curve measurement for resin flow in glass fibre reinforcement. *Compos Part A Appl Sci Manuf*. 2012;43:333-343. doi:10.1016/j.compositesa.2011.12.001
22. LeBel F, Ruiz E, Trochu F. Void content analysis and processing issues to minimize defects in liquid composite molding. *Polym Compos*. 2017;40:109-120. doi:10.1002/pc
23. Facciotto S, Simacek P, Advani SG, Middendorf P. Modeling of anisotropic dual scale flow in RTM using the finite elements method. *Compos Part B Eng*. 2021;214:108735. doi:10.1016/j.compositesb.2021.108735
24. LeBel F, Ruiz E, Trochu F. Experimental study of saturation by visible light transmission in dual-scale fibrous reinforcements during composite manufacturing. *J Reinf Plast Compos*. 2017;36:1693-1711. doi:10.1177/0731684417725187
25. Yoshihara K, Kamei Y, Mizuno A, Ohgaki H, Hori T, Ueno I. Effect of wettability on viscous fluid impregnation in single-layer woven-fibre bundles driven by pressure difference. *Compos Part A Appl Sci Manuf*. 2020;138:106049. doi:10.1016/j.compositesa.2020.106049
26. Matsuzaki R, Naito M, Seto D, Todoroki A, Mizutani Y. Analytical prediction of void distribution and a minimumvoid angle in anisotropic fabrics for radial injection resin transfer molding. *Express Polym Lett*. 2016;10:860-872. doi:10.3144/expresspolymlett.2016.80
27. Zhao C, Yang B, Wang S, Ma C, Wang S, Bi F. Three-dimensional numerical simulation of meso-scale-void formation during the mold-filling process of LCM. *Appl Compos Mater*. 2019;26:1121-1137. doi:10.1007/s10443-019-09770-w
28. Schmachtenberg E, Heide J, Töpker J. Application of ultrasonics for the process control of resin transfer moulding (RTM). *Polym Test*. 2005;24:330-338. doi:10.1016/j.polymertesting.2004.11.002
29. Stöven T, Weyrauch F, Mitschang P, Neitzel M. Continuous monitoring of three-dimensional resin flow through a fibre preform. *Compos Part A Appl Sci Manuf*. 2003;34:475-480. doi:10.1016/S1359-835X(03)00059-9
30. Thomas S, Bongiovanni C, Nutt SR. In situ estimation of through-thickness resin flow using ultrasound. *Compos Sci Technol*. 2008;68:3093-3098. doi:10.1016/j.compscitech.2008.07.012
31. Konstantopoulos S, Grössing H, Hergan P, Weninger M, Schledjewski R. Determination of the unsaturated through-thickness permeability of fibrous preforms based on flow front detection by ultrasound. *Polym Compos*. 2018;39:360.
32. Leisen J, Beckham HW. Void structure in textiles by nuclear magnetic resonance, part I. Imaging of imbibed fluids and image analysis by calculation of fluid density autocorrelation functions. *J Text Inst*. 2008;99:243-251. doi:10.1080/00405000701404122
33. Neacsu V, Leisen J, Beckham HW, Advani SG. Use of magnetic resonance imaging to visualize impregnation across aligned cylinders due to capillary forces. *Exp Fluids*. 2007;42:425-440. doi:10.1007/s00348-007-0251-0
34. Endruweit A, Glover P, Head K, Long AC. Mapping of the fluid distribution in impregnated reinforcement textiles using magnetic resonance imaging: application and discussion. *Compos Part A Appl Sci Manuf*. 2011;42:1369-1379. doi:10.1016/j.compositesa.2010.11.012
35. Teixidó H, Caglar B, Revol V, Michaud V. In-operando dynamic visualization of flow through porous preforms based on x-ray phase contrast imaging. *Compos Part A Appl Sci Manuf*. 2021;149:106560. doi:10.1016/j.compositesa.2021.106560
36. Teixidó H, Broggi G, Caglar B, Michaud V. Measurement and modelling of dynamic fluid saturation in carbon reinforcements. *Compos Part A*. 2023;169:107520.
37. Vilà J, Sket F, Wilde F, Requena G, González C, LLorca J. An in situ investigation of microscopic infusion and void transport during vacuum-assisted infiltration by means of x-ray computed tomography. *Compos Sci Technol*. 2015;119:12-19. doi:10.1016/j.compscitech.2015.09.016
38. Larson NM, Zok FW. Insights from in-situ x-ray computed tomography during axial impregnation of unidirectional fiber beds. *Compos Part A Appl Sci Manuf*. 2018;107:124-134. doi:10.1016/j.compositesa.2017.12.024
39. Larson NM, Cuellar C, Zok FW. X-ray computed tomography of microstructure evolution during matrix impregnation and curing in unidirectional fiber beds. *Compos Part A Appl Sci Manuf*. 2019;117:243-259. doi:10.1016/j.compositesa.2018.11.021
40. Castro J, Sket F, González C. S-XCT experimental determination of local contact angle and meniscus shape in liquid moulding of composites. *Compos Sci Technol*. 2020;199:108362. doi:10.1016/j.compscitech.2020.108362
41. Castro J, Sket F, Helfen L. In situ local imaging and analysis of impregnation during liquid moulding of composite materials using synchrotron radiation computed laminography. *Compos Sci Technol*. 2021;215:108999. doi:10.1016/j.compscitech.2021.108999
42. Michaud VJ, Compton LM, Mortensen A. Capillarity in isothermal infiltration of alumina fiber preforms with aluminum. *Metall Mater Trans A*. 1994;25:2145-2152.
43. Caglar B, Tekin C, Karasu F, Michaud V. Assessment of capillary phenomena in liquid composite molding. *Compos Part A Appl Sci Manuf*. 2019;120:73-83. doi:10.1016/j.compositesa.2019.02.018
44. Neitzel B, Puch F. Optical detection of void formation mechanisms during impregnation of composites by UV-reactive resin systems. *J Compos Sci*. 2022;6:1-15.
45. Malik MS, Schlögl S, Wolfahrt M, Sangermano M. Review on UV-induced cationic frontal polymerization of epoxy monomers. *Polymers (Basel)*. 2020;12:2146. doi:10.3390/polym12092146
46. Sangermano M, Razza N, Crivello JV. Cationic UV-curing: technology and applications. *Macromol Mater Eng*. 2014;299:775-793. doi:10.1002/mame.201300349
47. Crivello JV, Liu S. Free radical induced acceleration of cationic photopolymerization. *Chem Mater*. 1998;10:3724-3731. doi:10.1021/cm980494n
48. Staal J, Caglar B, Hank T, et al. In-series sample methodology for permeability characterization demonstrated on carbon nanotube-grafted alumina textiles. *Compos Part A Appl Sci Manuf*. 2021;150:106631. doi:10.1016/j.compositesa.2021.106631

49. Salvatori D, Caglar B, Teixidó H, Michaud V. Permeability and capillary effects in a channel-wise non-crimp fabric. *Compos Part A*. 2018;108:41-52. doi:10.1016/j.compositesa.2018.02.015
50. Sket F, Enfedaque A, Alton C, González C, Molina-Aldareguia JM, Llorca J. Automatic quantification of matrix cracking and fiber rotation by x-ray computed tomography in shear-deformed carbon fiber-reinforced laminates. *Compos Sci Technol*. 2014;90:129-138. doi:10.1016/j.compscitech.2013.10.022
51. Staal J, Smit E, Caglar B, Michaud V. Thermal management in radical induced cationic frontal polymerisation for optimised processing of fibre reinforced polymers. *Compos Sci Technol*. 2023;237:110009.
52. Chen B, Chou TW. Compaction of woven-fabric preforms: nesting and multi-layer deformation. *Compos Sci Technol*. 2000;60:2223-2231. doi:10.1016/S0266-3538(00)00017-8
53. Yousaf Z, Potluri P, Withers PJ. Influence of tow architecture on compaction and nesting in textile preforms. *Appl Compos Mater*. 2017;24:337-350. doi:10.1007/s10443-016-9554-8
54. Teixidó H, Caglar B, Michaud V. Effect of wettability and textile architecture on fluid displacement and pore formation during infiltration of carbon fibrous preforms. *Compos Part A Appl Sci Manuf*. 2023;174:107733. doi:10.1016/j.compositesa.2023.107733

SUPPORTING INFORMATION

Additional supporting information can be found online in the Supporting Information section at the end of this article.

How to cite this article: Staal J, Caglar B, Michaud V. A methodology for microstructural evaluation of unsaturated flow phenomena by in-situ UV-flow freezing. *Polym Compos*. 2024;1-13. doi:10.1002/pc.29448